Carbon 148 (2019) 277–289

Contents lists available at ScienceDirect

Carbon

journal homepage: www.elsevier.com/locate/carbon

The roles of metal-organic frameworks in modulating water permeability of graphene oxide-based carbon membranes

Xiao Sui [a, 1], Hongru Ding [a, b, 1, 2], Ziwen Yuan [a], Chanel F. Leong [c], Kunli Goh [d, e], Wei Li [a], Nuo Yang [b], Deanna M. D'Alessandro [c], Yuan Chen [a, *]

[a] The University of Sydney, School of Chemical and Biomolecular Engineering, Sydney, NSW, 2006, Australia
[b] School of Energy and Power Engineering, Huazhong University of Science and Technology, Wuhan, 430074, PR China
[c] The University of Sydney, School of Chemistry, Sydney, NSW, 2006, Australia
[d] Singapore Membrane Technology Centre, Nanyang Environment and Water Research Institute, Nanyang Technological University, Singapore, 637141, Singapore
[e] School of Chemical and Biomedical Engineering, Nanyang Technological University, Singapore, 637459, Singapore

ARTICLE INFO

Article history:
Received 21 December 2018
Received in revised form
16 March 2019
Accepted 20 March 2019
Available online 25 March 2019

Keywords:
Graphene oxide
Metal-organic framework
Membrane
Water permeability
Molecular simulation

ABSTRACT

Graphene oxide (GO) can be processed into carbon membranes with unique water permeability and molecular selectivity. Metal-organic frameworks (MOFs) have been proposed as filler materials to enhance water permeability of laminar GO-based carbon membranes. However, it remains unclear how the enhancement arises. Herein, we combined experimental and molecular simulation studies to provide critical insights into the water transport behaviors of GO/MOF composite membranes. The water permeability enhancement was found to be directly correlated to the increase in the average interlayer spacing between GO nanosheets. The simulation results indicate a slower water transport through nanochannels in MOFs than in nanochannels formed by GO nanosheets. A small amount of MOF particles only serves as a blockage in laminar GO membranes, suppressing their water permeability. In contrast, a large amount of MOF particles increases the interlayer spacing between GO nanosheets and creates very fast water transport stretches. Besides, some large gaps are formed between non-smooth MOF particles and GO nanosheets, adding supplementary water channels to deliver higher water permeability. We envision a shift in future research direction to exploit the selective adsorption capacity of MOFs other than leveraging them as fast water transport channels to realize their potential water treatment applications.

1. Introduction

Owing to their unique one-atom-thick 2D structure and tunable physicochemical properties, graphene materials represent a potential candidate material in fabricating advanced carbon membranes for separation applications, such as pervaporation, gas separation, water treatment, and desalination [1–9]. In particular, graphene oxide (GO) possesses excellent processability and stability in aqueous solutions [10–12], allowing facile assemblies into laminar membranes with promising water permeability and molecular selectivity properties [3,4,13,14]. The separation mechanism depends on a tortuous pathway created by the impermeable lamellar GO nanosheets [15–18], which offer size-exclusion effects through the interlayer spacing between the nanosheets. Besides, selective interactions by the functional groups on the GO nanosheets may play a significant role [18–21]. From a membrane perspective, the interlayer spacing between adjacent GO nanosheets serves as membrane pores, which critically influence the separation performance of GO membranes [14,16,22,23]. Dried and tightly packed GO membranes may have an interlayer spacing of ~0.3 nm similar to that of graphite, which would only allow a monolayer of water vapor to permeate through [15]. In contrast, hydrated and expanded GO membranes can possess significantly larger interlayer spacing up to several nanometers [4,15,24], suggesting that the interlayer spacing of GO membranes can be engineered [15,25]. To date, a multitude of nanomaterials with different

* Corresponding author.
E-mail address: yuan.chen@sydney.edu.au (Y. Chen).
[1] These authors contributed equally to this work.
[2] Current address: Department of Mechanical Engineering, The University of Texas at Austin, E. Dean Keeton Street, Austin, TX 78712, USA.

https://doi.org/10.1016/j.carbon.2019.03.049
0008-6223/

dimensions has been explored as nanospacers for this purpose [26–31]. For example, the water permeability of GO membranes intercalated with carbon dots was 9 times higher than that of pristine GO membranes while retaining similar dye removing efficiency [26]. Multi-walled CNTs (MWCNTs) were also used as spacers to prevent the collapse of nanochannels under pressure and enhance the stability of GO membranes [27,28].

Metal-organic frameworks (MOFs) are crystalline materials constructed from inorganic metal centers and organic ligands. They are deemed attractive for separation applications because of their adjustable and designable pore sizes and chemical functionalities, which can provide selective solute transport [32]. MOFs have been extensively studied for gas and organic mixture separation [33–39], as well as water treatment applications. However, there are only a few MOFs such as ZIF-8 (zeolitic imidazolate frameworks) and UiO-66, which are water-stable and have shown good selectivity towards alkali metal ions in water treatment [24,25,37,38,40,41]. These early studies have reported that MOF-intercalated GO membranes could achieve higher water permeability without sacrificing their selectivity [24,25,37,38,40,41]. For example, the water permeability of MOF (*i.e.* UiO-66) intercalated reduced GO membranes was reported to be 15 times higher than that of pristine reduced GO membranes with a similar dye rejection rate [30]. It has been proposed that the higher water permeability can be attributed to additional water transport nanochannels through intrinsic pores of MOF particles. However, these assumptions have yet to be confirmed.

Hence, this work aims to explore the effect of MOF intercalation and elucidate how water transport behaviors vary in lamellar GO-based carbon membranes. We selected two zirconium-based MOFs, *i.e.* MIL-140A and UiO-66, considering their structural morphology, pore sizes, hydrophilicity, and chemical stability, which originated from the strong bonding between the high valent Zr(IV) ions and carboxylates [40,42]. GO/MOF composite membranes were fabricated by a typical filtration method. The effect of MOF intercalation on the water permeability was experimentally studied in tandem with water transport simulations in nanochannels of MOFs or between GO nanosheets with different interlayer spacing using molecular dynamic (MD) simulations. Our results reveal that water transport in nanochannels of MOFs is much slower than in nanochannels between GO nanosheets and provide unique insights into the effects of MOF-based nanoscale spacers in GO membranes for water treatment.

2. Experimental section

2.1. Materials

GO aqueous dispersion (Graphenea, 2.5 wt% highly concentrated GO) was first diluted using deionized water as a stock solution at the concentration of 0.5 mg/mL. Polycarbonate (PC) membranes (Millipore, 0.2 μm pore size, 47 mm diameter) were used as the membrane substrates. Zirconium (IV) chloride ($ZrCl_4$, Sigma-Aldrich, >99.5%) and 1,4-benzenedicarboxylic acid (H_2bdc, Sigma-Aldrich, 98%), Acetic acid (Univar Ajax Finechem, 99.9%) and N, N′- dimethylformamide (DMF, Univar Ajax Finechem, >99.5%) were used as received without further purification.

2.2. Synthesis of MOFs

MIL-140A was synthesized by a microwave-assisted method [43]. Briefly, 0.25 mmol $ZrCl_4$ was mixed with 0.5 mmol H_2bdc before adding 0.04 mL (0.7 mmol) of acetic acid and 2.5 mL of DMF. The mixture was heated to 220 °C in 2 min under magnetic stirring in a microwave oven (Anton Paar Monowave 300) and then held at 220 °C for 15 min before cooled to 55 °C in 2 min. The resulting solid precipitates were collected by vacuum filtration and then washed by DMF and acetone several times. Subsequently, the solid materials were solvent exchanged with methanol using a Soxhlet washing procedure for 12 h before being dried in a vacuum oven. An acetic-acid mediated solvothermal-method was used to synthesize UiO-66 [42]. Briefly, 0.25 mmol of $ZrCl_4$ was mixed with 0.25 mmol H_2bdc before adding 1.75 mmol (0.1 mL) of acetic acid and 2.5 mL of DMF. The mixture was sonicated for 10 min to obtain a clear solution. Subsequently, the clear solution was heated at 120 °C in a hydrothermal autoclave and kept at the temperature for 16 h. The resulting solid precipitates were collected by vacuum filtration. Dried powders were obtained using the same purification procedure as used for MIL-140A.

2.3. Membrane fabrication

The GO/MOF composite membranes were fabricated by pressure-assisted filtration. A diluted aqueous GO dispersion (0.005 mg mL $^{-1}$, 40 mL) was first prepared from the GO stock solution and bath-sonicated for 30 min. Next, aqueous MOF dispersions were prepared by dispersing different amounts of MIL-140A or UiO-66 (ranging from 10, 20, 30 to 50 wt%) in 10 mL deionized water using bath sonication at 25 °C for 30 min. The MOF dispersion was added into the 40 mL GO dispersion under stirring at the room temperature for 30 min to form GO/MOF mixtures. The GO/MOF mixture was filtrated on a PC membrane (17.35 cm^2 area) under 1 bar pressure using a dead-end filtration cell (Sterlitech, HP4750). GO membranes were also prepared as a control. 40 mL of diluted aqueous GO dispersion was filtered without MOFs. It should be noted that the mass loading of GO on all membranes was kept the same at 0.2 mg. Once the filtration completed, the as-prepared membranes were immediately dried by an Ar gas flow at 1 bar pressure in the dead-end filtration cell.

2.4. Evaluation of water permeability

The water permeability was measured using a dead-end filtration cell under an applied pressure (1 bar) in Ar gas. The membranes were first compressed for 30 min under 1 bar, and then the permeate was collected in 5 min and weighed using a digital balance. The pure water permeability (PWP) was calculated according to Eq. (1):

$$\mathrm{PWP} = \frac{V}{tA\Delta P} \tag{1}$$

where V (L) is the volume of the permeate collected, t (h) is the permeation time, A (m^2) is the effective membrane surface area (8.04 cm^2) and ΔP (bar) is the 1 bar pressure applied to the membrane.

2.5. Material characterization

The morphology of MIL-140A and UiO-66 was examined by a field emission SEM (Zeiss, Ultra Plus). The surface elemental compositions were determined by energy-dispersive X-ray spectroscopy (EDS). The crystallinity of MOF particles and the d-spacing of GO/MOF composite membranes were determined by X-ray diffraction (XRD) on XRD diffractometer (PANalytical X'pert Pro) equipped with a solid-state detector (40 kV, 30 mA, 1° divergence and anti-scatter slits, and 0.3 mm receiver and detector slits) and a Cu-Kα (λ = 1.5406 Å) X-ray source. The N_2 physisorption isotherms were measured using a surface characterization analyzer (Micromeritics, 3Flex). 100 mg of powder samples were loaded into a glass

analysis tube and outgassed for 12 h under vacuum at 120 °C before measurement. N_2 adsorption and desorption isotherms were obtained at 77 K. The specific surface area was calculated using the Brunauer–Emmett–Teller (BET) method and the pore size distribution was calculated based on the density functional theory (DFT) model. The chemical characteristics of GO were investigated using a Raman spectrometer (Renishaw, inVia Reflex) equipped with a 785 nm laser. The lateral dimension of GO nanosheets was examined by atomic force microscope (AFM, Asylum Research, MFP-3D) in the AC mode. The water contact angle of the membranes was measured using a drop shape analyzer (Krűss, DSA 25).

2.6. Computational methods

Structural models of water in GO, MIL-140A and UiO-66 channels is illustrated in Fig. 1. GO model consists of C atoms forming the 2D carbon framework, and surface carboxyl, carbonyl, and hydroxyl groups. The density of surface functional groups is set as the same as their concentration on GO nanosheets used in this study as determined by XPS (Fig. S1 in the SI). $n_{COOH}/n_C = 0.07$, $n_{C=O}/n_C = 0.09$, and $n_{OH}/n_C = 0.43$, respectively, where n_{COOH}, $n_{C=O}$, n_{OH}, and n_C are the number of carboxyl, carbonyl, and hydroxyl groups, and carbon atoms in the GO model, respectively. MIL-140A is formed by zirconium oxide chains units linked by terephthalate linkers leading to a pore diameter of 3.2 Å and has a chemical formula of $[ZrO(O_2CC_6H_4CO_2)]$. It contains triangular-shaped pore channels (Fig. 1b–d) [44]. UiO-66 (Fig. 1e–f) consists of $Zr_6O_4(OH)_4$ clusters as inorganic subunits, which are each 12-fold bridged to other nodes via the benzene 1,4-dicarboxylate linker, resulting in triangular windows with a size of 6 Å. These windows connect two types of cages (octahedral: 11 Å Ø; tetrahedral: 8 Å Ø) [45].

Molecular dynamic simulations were carried out using the LAMMPS code [46,47], with a time step of 0.8 fs at room temperature. Periodic boundary conditions were applied in all directions. The dimension of the simulation boxes for GO, MIL-140A, and UiO-66 (including two simulation cells) is $50 \times 23 \times 30$ Å, $61 \times 23 \times 24$

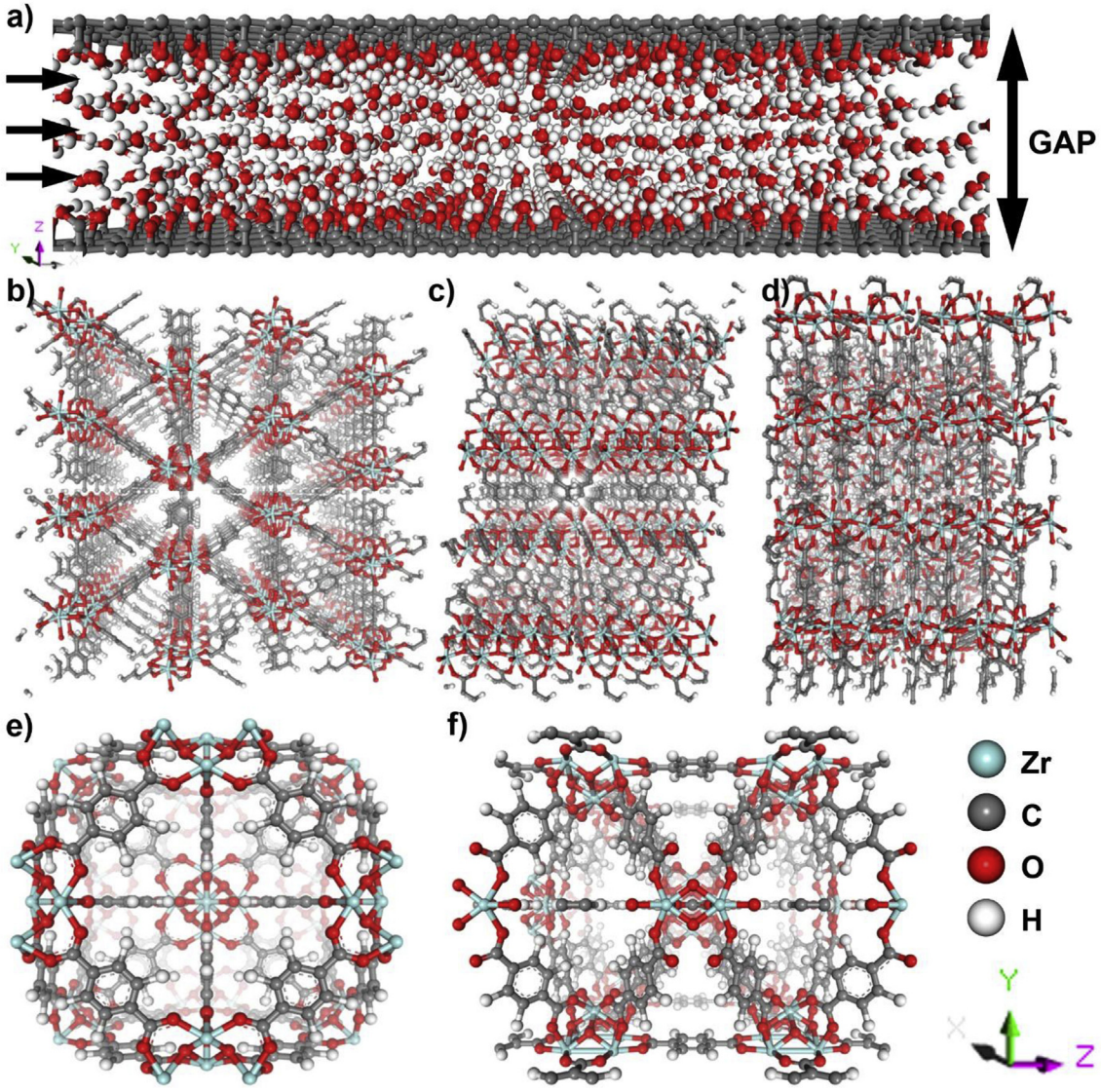

Fig. 1. MD simulation models of water transport in nanochannels formed by (a) GO, (b–d) MIL-140A, and (e–f) UiO-66. Pressures are applied along + x axis in all simulations. (b–f) water transports along different directions in nanochannels of MOFs: (b–d) the direction 1, 2, 3 of MIL-140A, respectively; and (e–f) the direction 1, 2 of UiO-66, respectively. Zr, C, O, and H atoms are in cyan, grey, red and white color, respectively. The axis indicator of (b–f) is shown in the bottom right corner. Water molecules are not shown in MOF models to obtain clearer figures. (A colour version of this figure can be viewed online.)

Å, 61 × 21 × 29 Å and 61 × 21 × 21 Å, respectively. The rigid TIP4P model was used for water molecules[58]. All-atom optimized potentials for liquid simulations (OPLS-AA) force field were used in all simulation [48,49]. The LJ parameters and atomic partial charges of MIL-140A and UiO-66 were taken from the universal force field (UFF) and the DREIDING force field [50,51] and density function theory [52], respectively. The long-range electrostatic forces were computed with the P^3M method. For all pairwise LJ terms, Lorentz-Berthelot mixing rule was applied. The cut-off distance in the LJ potential was set to 2.5 σ. In all simulations, to reduce the computational cost, we assumed all the membrane atoms were held rigid. The potential parameters of atoms are listed in the Supporting Information. Non-equilibrium molecular dynamics (NEMD) simulations in canonical ensemble (NVT) were used to record simulation data after the structure relaxation in the NVT ensemble. Nosé–Hoover thermostats were applied to water molecules. To obtain meaningful statistics, for each set of parameters, 8 independent simulations were performed for a sufficiently long time (8 ns). In all simulations, the MOFs were assumed to be rigid in order to oppose the applied external force and prevent them from drifting [53,54]. Hydraulic pressure was applied by directly adding forces to water molecules. We first obtained 2D water density profiles and velocity profiles in GO or MOF channels. Next, their 2D mass flux rate profiles were obtained by combing water density profiles and velocity profiles. The areal average of mass flux rates in GO or MOF channels was then calculated as the water permeability rate in each channel.

3. Results and discussion

3.1. Fabrication of GO/MOF composite membranes

Commercial GO solutions were used to fabricate laminar GO membranes. Within the GO membranes, two types of MOFs (MIL-140A and UiO-66) with distinctive morphologies served as the intercalated spacers. MIL-140A has a plate-like structure, while UiO-66 has a spherical structure. They were synthesized as described in the experimental section [42,43]. The composite membranes were fabricated by a pressure-assisted filtration method (Fig. 2), which is well-known for producing GO laminates with a highly ordered microstructure [27,31,55]. MIL-140A or UiO-66 solutions were first mixed with diluted GO dispersion in MOF to GO weight ratios of 0.1, 0.2, 0.3 and 0.5. The mixtures were then filtered on a polycarbonate (PC) membrane substrate under 1 bar of Ar gas to yield GO/MOF composite membranes (denoted as GO/MOF–*x*, where *x* refers to the weight ratio between MOF and GO).

The crystallinity of synthesized MOF particles was characterized by XRD, their XRD profiles (Fig. 3a) consistent with those reported in previous studies [42,43]. The morphology of MOF particles was examined by scanning electron microscope (SEM). Fig. 3b shows that MIL-140A exhibits a plate-like structure with a plate thickness of 60–70 nm and a lateral dimension of ~0.8–2 μm. In contrast, UiO-66 is spherical with a particle size of 60–70 nm (Fig. 3c). The Brunauer–Emmett–Teller (BET) specific surface areas of MIL-140A and UiO-66 are 449.2 and 1210.4 m^2/g, respectively, as measured by N_2 physisorption (Fig. S2 in the Supplementary data, SD). The pore size distribution analysis indicates that the pores of UiO-66 are in the range of 0.8–1.6 nm, and MIL-140A exhibits a pore size of 0.9 nm. As shown in Fig. S3 in the SD, GO nanosheets used in this study have a mean lateral dimension of ~2 μm, which is much larger than that for individual UiO-66 particles and many MIL-140A particles. The Raman spectrum (Fig. S4 in the SD) shows an intense D band, indicating defective graphitic structures and thus the existence of abundant surface functional groups on GO nanosheets. In order to obtain reliable results, all the GO solutions were prepared with the same treatment to ensure the consistency of the physicochemical properties of GO solutions used in each membrane.

SEM also examined the fabricated GO/MOF composite membranes. Fig. 4a shows the surface of the PC substrates, with pores of about 0.2 μm. Fig. 4b illustrates the surface morphology of a GO membrane, revealing wrinkles which can be attributed to the hydrogen bonds between hydrophilic groups on the basal planes and edges of GO nanosheets [56–58]. The top views of GO/MIL-140A–0.5 and GO/UiO-66–0.5 membranes are shown in Fig. 4c and d, respectively. The plate-like structure of the MIL-140A and the spherical structure of the UiO-66 are visible under the GO layer. In addition to wrinkles originating from the GO nanosheets, more wrinkles can be observed around MOF particles. These wrinkles

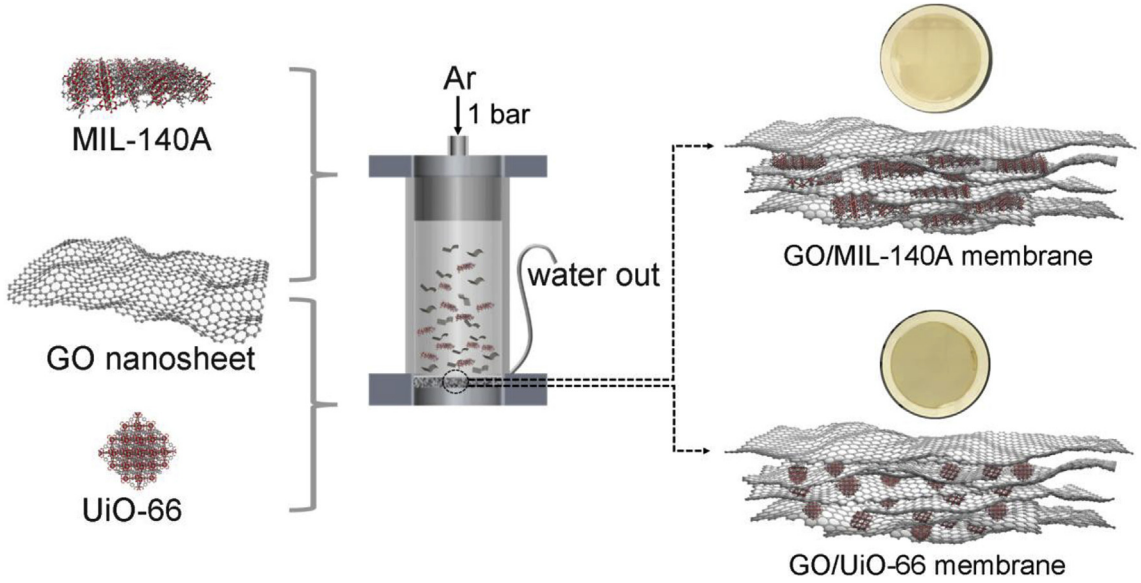

Fig. 2. Schematic illustration of the fabrication of GO/MOF composite membranes by the pressure assisted filtration method (photos of GO/MOF composite membranes are shown together with their structural illustrations). (A colour version of this figure can be viewed online.)

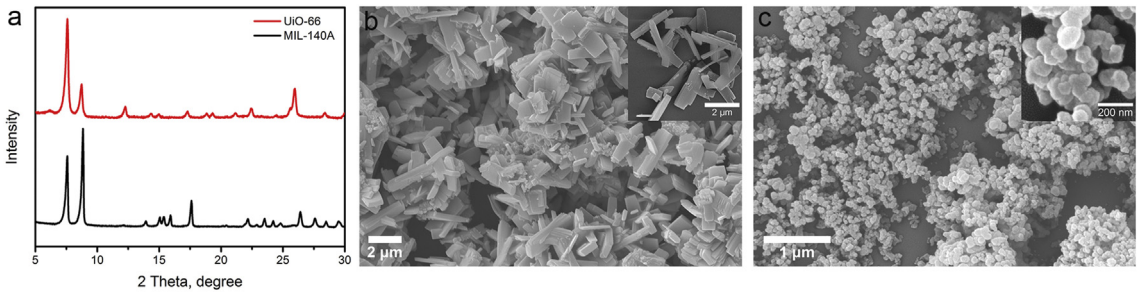

Fig. 3. (a) XRD spectra and SEM images of (b) MIL-140A and (c) UiO-66. The inserts in (b–c) show their corresponding enlarged SEM images. (A colour version of this figure can be viewed online.)

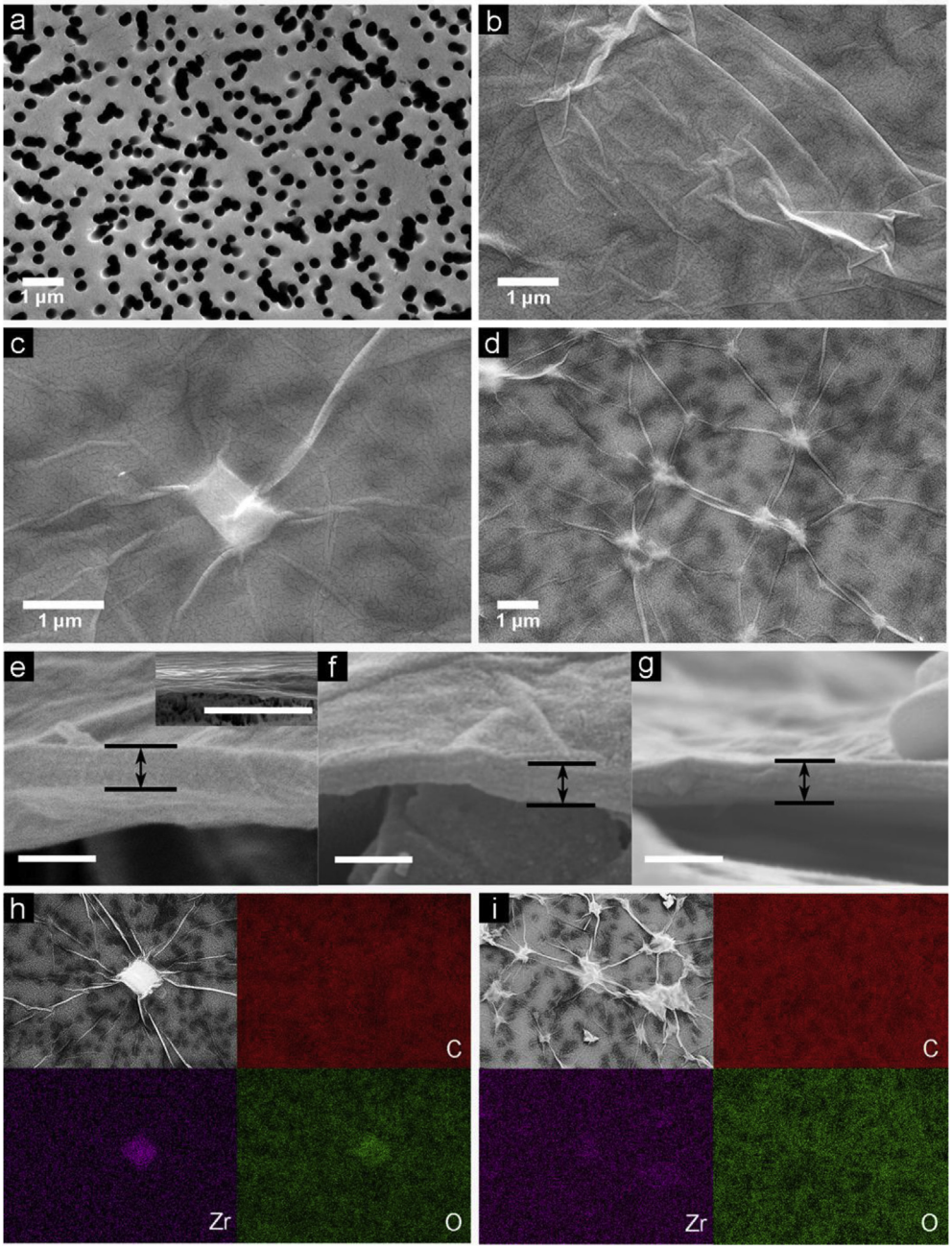

Fig. 4. SEM images of the top views of (a) the polycarbonate membrane substrate, (b) GO, (c) GO/MIL-140A–0.5, and (d) GO/UiO-66–0.5 membranes. SEM images of the cross-sectional views of (e) GO (the scale bar in the inserted image is at 1 μm), (f) GO/MIL-140A–0.5, and (g) GO/UiO-66 membranes (the scale bars in (e, f, and g) are at 200 nm). SEM images and the corresponding EDS mappings of (h) GO/MIL-140A–0.5 and (i) GO/UiO-66–0.5 membranes. (A colour version of this figure can be viewed online.)

spread out evenly over the entire membrane surface. Their even distribution over the entire membrane surface suggests that the embedded MOF particles exhibit minor aggregations (Fig. 4c and d). The cross-sectional membrane morphologies are shown in Fig. 4e–g. The GO membrane contains densely stacked GO nanosheets with a thickness of 200 nm. Surprisingly, GO/MIL-140A–0.5 and GO/UiO-66–0.5 membranes demonstrate similar thickness despite MOF particles intercalation. This suggests moderate alterations to the interlayer distance between GO nanosheets.

EDS analyzed the surface elemental composition of GO/MOF membranes. Fig. 4h and i show that the C and O elements are distributed uniformly on the membrane surfaces. The Zr mappings corroborate the presence of MIL-140A and UiO-66 particles. The hydrophilicity of the GO/MOF composite membrane surfaces was quantified by measuring their water contact angles. Fig. S5 in the SD shows a minor decrease in the contact angle of the GO/MOF composite membranes with an increase in the MOF to GO mass ratio, indicating similar surface hydrophilicity to that of the GO membrane. These characterizations demonstrate uniform interaction of the MOF particles without compromising the structural integrity of the GO membranes.

3.2. Water permeability of GO/MOF composite membranes

Water permeability (L m $^{-2}$ h $^{-1}$) of GO and GO/MOF composite membranes was measured under 1 bar applied pressure as described in the experimental session, with results presented as their water permeability coefficients (L m $^{-2}$ h $^{-1}$ bar $^{-1}$). At least three separate measurements were performed for every membrane to obtain reliable results. It should be noted that water transport here is under the pressure-driven permeation mode. The role of capillary pressures is minor because there are no phase changes on the permeate side under the pressure-driven permeation mode [59,60]. Therefore, the water permeation should only depend on the applied hydraulic pressure. As shown in Fig. 5, pristine GO membranes have a water permeability coefficient of 7.8 L m $^{-2}$ h $^{-1}$ bar $^{-1}$. With the addition of MIL-140A, the water permeability coefficient of GO/MIL-140A–0.1 decreases to 4.9 L m $^{-2}$ h $^{-1}$ bar $^{-1}$ before elevating with increasing mass loading of MIL-140A. GO/MIL-140A–0.3 exhibits a similar water permeability coefficient to that of GO membranes, while the water permeability of GO/MIL-140A–0.5 increases to 14.8 L m $^{-2}$ h $^{-1}$ bar $^{-1}$, which is a 90% enhancement over the GO membranes. On the other hand, the water permeability coefficients of GO/UiO-66–0.1 and GO/UiO-66–0.2 are similar to that of GO membranes. GO/UiO-66–0.3 and GO/UiO-66–0.5 have water permeability coefficients of 14.9 and 15.0 L m $^{-2}$ h $^{-1}$ bar $^{-1}$, respectively, which are about two times the value of GO membrane. A noteworthy observation is a slight drop in water permeability coefficients of GO/MIL-140A–0.1 and GO/MIL-140A–0.2, which is missing in GO/UiO-66–0.1 and GO/UiO-66–0.2.

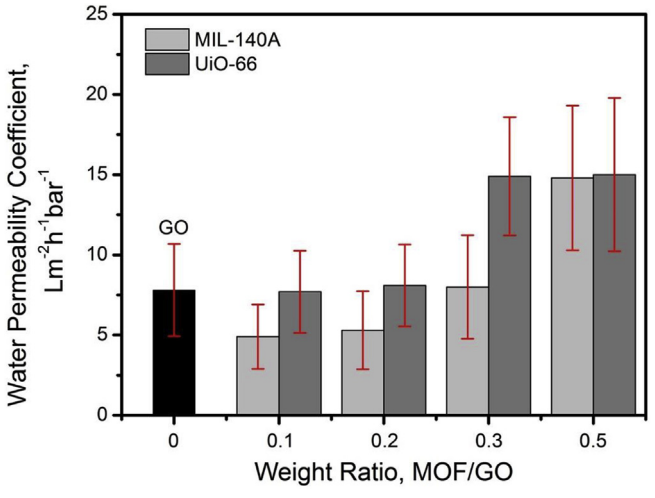

Fig. 5. Water permeability coefficients of GO and GO/MOF (MIL-140A or UiO-66) composite membranes with different MOF/GO ratios. The mass of GO in all membranes is the same. (A colour version of this figure can be viewed online.)

We also measured the molecular sieving capacity of these membranes. As shown in Fig. S6 in the SD, they demonstrated a rejection rate in the range of 68–81% for methylene blue ($MB+$) dyes, which is similar to a recently reported study [27]. To further increase their rejection rates, the membranes can be reduced to yield rGO/MOF composite membranes. For example, we also prepared a rGO/MIL-140–0.5 membrane with an elevated MB^{+} rejection rate of 95%. However, this increase in the rejection rate was accompanied by a decrease in water permeability coefficient from 3.2 to 0.2 L m^{-2} h^{-1} bar^{-1}. Since the main purpose of this study is to elucidate the roles of MOFs in enhancing water permeability of GO membranes, we focused our efforts on GO/MOF composite membranes other than improving their rejection performances.

To understand the water permeability coefficients, XRD was applied to investigate the average interlayer spacing of the GO/MOF composite membranes. Fig. 6 shows the GO characteristic peak at $2\theta = 10.44^{\circ}$, which corresponds to an interlayer spacing of 0.85 nm. For GO/MIL-140A, the same peak, however, gradually shifts to a lower angle with an increase in MIL-140A weight fraction, suggesting that the corresponding interlayer spacing of GO/MIL-140A–0.5 increases to 0.92 nm. A similar peak-shifting trend can be observed on GO/UiO-66 composite membranes. The corresponding interlayer spacing of GO/UiO-66 composite membranes increases from 0.85 to 0.92 nm when the weight ratio of UiO-66 to GO increases from 0.1 to 0.5. These observations suggest that intercalating MOF nanoparticles can modulate the interlayer spacing of GO nanosheets and a larger interlayer spacing can be created with an increase in the loading of MOF particles. It is noteworthy to mention that the MOF intercalated GO membranes remain relatively stable in water during our water permeability measurements. Fig. S7 in the SD shows the XRD patterns of GO/UiO-66-0.5 and GO/MIL-140A-0.5 and composite membranes before and after water permeability measurements. Peaks corresponding to the interlayer spacing show insignificant changes upon exposure to water. We speculated that multivalent cationic metal ions remained in GO nanosheets and ion residues from MOF particles may have helped to partially crosslink GO nanosheets to improve their stability in water [61].

3.3. MD simulations of water transport in nanochannels

MD simulations of water transport in nanochannels formed by GO, MIL-140A, and UiO-66 are illustrated in Fig. 1. The model in Fig. 1a shows a nanochannel formed by two parallel GO nanosheets consisting of surface carboxyl (COOH), carbonyl (C=O) and hydroxyl (OH) functional groups. The concentrations of these three types of functional groups are set to the same molecular ratios as determined by X-ray photoelectron spectroscopy (XPS) of the GO nanosheets used in this study (Fig. S1, SD). Specifically, $n_{COOH}/n_C = 0.07$, $n_{C=O}/n_C = 0.09$, and $n_{OH}/n_C = 0.43$, where n_{COOH}, $n_{C=O}$, n_{OH}, and n_C are the number of carboxyl, carbonyl, and hydroxyl groups, and carbon atoms in the GO model, respectively. MIL-140A is formed by zirconium oxide (ZrO_2) chains units linked by benzene-1,4-dicarboxylate linkers. Hence, it contains triangular-shaped pore channels of diameter 3.2 Å with a chemical formula of [$ZrO(O_2CC_6H_4CO_2)$] [44]. On the other hand, UiO-66 (Fig. 1e and

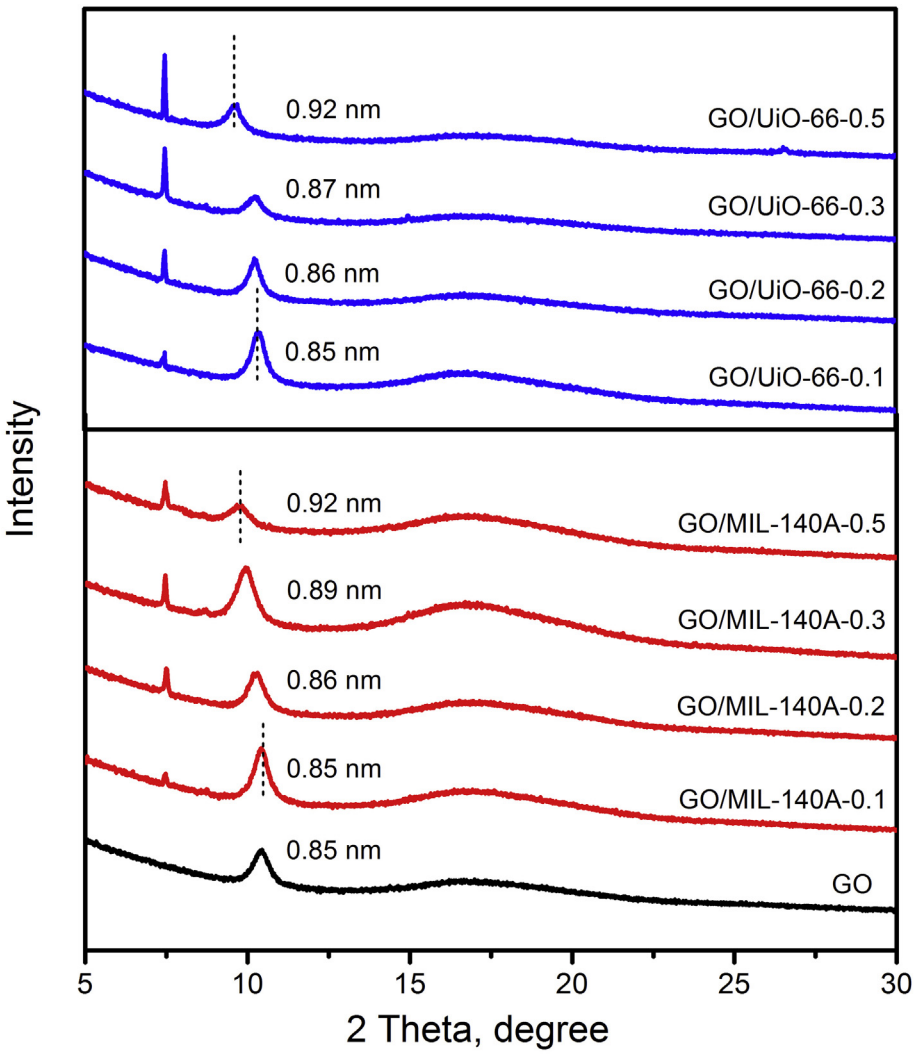

Fig. 6. XRD patterns of GO, GO/MIL-140A and GO/UiO-66 composite membranes with different MOF weight ratios. The calculated average interlayer distances between GO nanosheets are marked near XRD peaks. Peaks at $2\theta = 7.56^{\circ}$ belong to MIL-140A and UiO-66 crystals. (A colour version of this figure can be viewed online.)

f) consists of $Zr_6O_4(OH)_4$ clusters as inorganic subunits with benzene-1,4-dicarboxylate linkers. This results in triangular windows of size 6 Å connected to two types of cage (octahedral: 11 Å Ø; tetrahedral: 8 Å Ø) [45]. MIL-140A has three orientations, while UiO-66 has two orientations, which can form water transport nanochannels in different directions. Thus, we simulated water transport along the three orientations of MIL-140A and two orientations of UiO-66, as illustrated in Fig. 1b–f. The detailed MD method is described in the experimental section and the simulation parameters are listed in Table S1 in the SD. The density of water plays a crucial role in water transport within nanochannels [62]. Hence, to predict the equilibrium water density in the nanochannels, the GO nanochannels were simulated in a large water bath at a temperature of 300 K and a hydraulic pressure of 422 MPa. Likewise, the MOFs were placed in the water bath under 422 MPa to obtain the water density in the MOFs. The results are illustrated in Fig. S8 in the SD.

To simplify our simulation models, we used parallel GO nanochannels to simulate GO membranes in this study.

When water molecules pass through lamellar GO membranes, there are two major components in their traveling path: one is the gap among GO nanosheets or defects in GO nanosheets where water molecules move vertically downwards, and the other is nanochannels between two adjacent nanosheets where water molecules travel parallelly along the surface of GO nanosheets [53,63,64]. The size, morphological and chemical properties of GO nanosheets and their edges may influence the first component, while the membrane thickness would affect both components [18,60]. Considering that the GO membranes are thin, the distance traveled in the parallel part is much longer than the vertical part. In this study, we have used the same batch of GO nanosheets to fabricate all GO composite membranes. The GO nanosheets have a similar lateral size distribution and edge structures (see Fig. S3). Further, the same amount of GO (0.2 mg) was used in each membrane. Thus, we assume the contribution from the first component to the water transport is similar in all studied GO membranes. We focused on the second component. We first simulated the water transport in GO nanochannels with different interlayer spacings. Water flow in the nanochannels shows a Poiseuille flow characteristic with a parabolic velocity profile (Fig. S9, SD). Next, water permeability coefficients (■ in Fig. 7) were simulated for a series of interlayer spacing ranging from 0.82 to 1.06 nm. Results show a significant increase in water permeability coefficients from 5.5 to 33.2 L m^{-2} h^{-1} bar^{-1} with increasing interlayer spacing, indicating

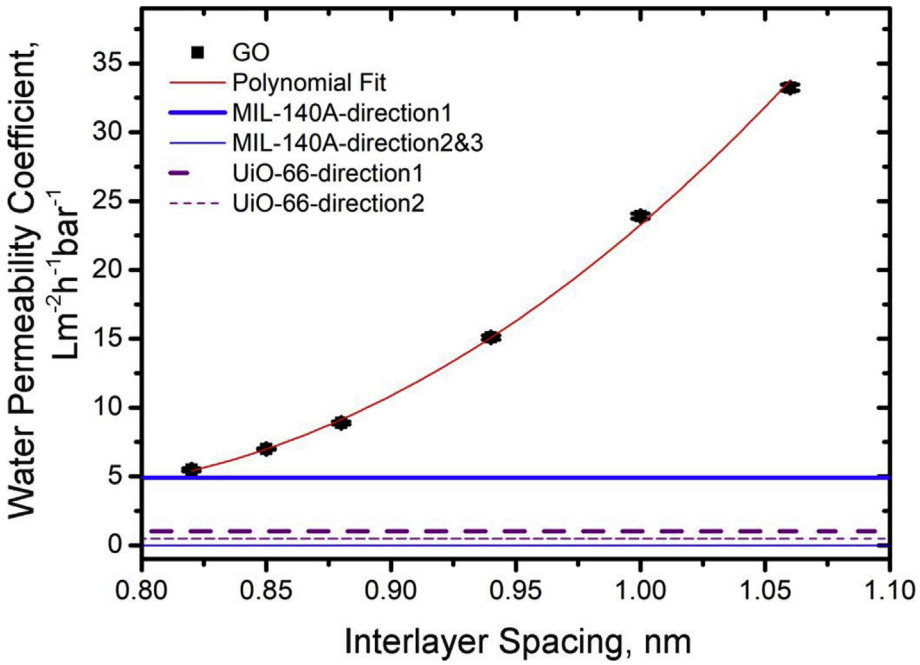

Fig. 7. Water permeability coefficients of nanochannels between two GO nanosheets (black dots), and in MIL-140A (blue lines) or UiO-66 (purple dash lines). The red line is a fitting line of water permeability coefficients of GO nanochannels. The thick blue line corresponds to water transport along direction 1 (+*x* axis of Fig. 1b) in MIL-140A, and the thin blue line corresponds to direction 2 and 3 (+*x* axis of Fig. 1 c–d). The thicker and thinner purple dash lines correspond to water transport along direction 1 (+*x* axis of Fig. 1e) and direction 2 (+*x* axis of Fig. 1f) in UiO-66, respectively. (A colour version of this figure can be viewed online.)

that the water permeability in GO nanochannels is highly sensitive to the interlayer spacing given that a 29% enlargement in the interlayer spacing causes a 517% enhancement in the water permeability.

The blue and purple dashed lines in Fig. 7 correspond to the water permeability coefficients of the nanochannels in MIL-140A and UiO-66 along different directions, respectively. For the three directions in MIL-140A (see Fig. 1b–d), the simulated water permeability coefficients are 4.9, 0 and 0 L m $^{-2}$ h $^{-1}$ bar $^{-1}$, respectively. As shown in Movie S1 in the SD, water molecules can pass through MIL-140A smoothly along direction 1 (Fig. 1b). However, no water molecules can enter MIL-140A along direction 2 or 3 (Fig. 1c and d) despite a three-time higher pressure (see Movie S2 in the SD). Thus, MIL-140A possesses only one effective water transport channel, and water molecules cannot pass through MIL-140A when pressure is applied perpendicular to the other two facets. In contrast, water molecules can penetrate UiO-66 in both simulated directions. The water permeability coefficients are 0.48 and 1.02 L m $^{-2}$ h $^{-1}$ bar $^{-1}$ along the two directions simulated for UiO-66 (Fig. 1e and f).

Fig. 7 shows that the water permeability coefficients in MOFs are much lower than that of the GO nanochannel with an interlayer spacing of 0.85 nm, except for direction 1 in MIL-140A. However, when MIL-140A nanoparticles are intercalated in the GO nanosheets, the pores are expected to orient randomly to the water flow direction. Hence, despite a theoretically higher water permeability coefficient from the direction 1 in MIL-140A, the observed water permeability coefficient is expectedly much lower due to the random orientation of the MIL-140A nanoparticles, which results in an overall lower average water permeability coefficient over the three directions. These simulation results indicate that MIL-140A and UiO-66 do not contribute to channels with faster water transport as compared to the original GO nanochannels.

We further investigated water density and velocity profiles in MOFs to better understand the water transport behavior in MOFs. Fig. 8 illustrates the water density and velocity profiles in MIL-140A (direction 1) and UiO-66 (direction 1 and 2), respectively. The vertical and horizontal axes correspond to the Y and Z axes, respectively, with pressures applied along the +X axis. The warmer color represents a higher water density in the density profile or higher velocity along the +X axis in the velocity profile. On the other hand, the cooler color in the velocity profile corresponds to a higher velocity along the -X axis. It should be noted that the blue regions shown in Fig. 8 are not equal to zero but indicate an extremely low velocity close to 0. This can be rationalized by considering the rich hydrophilic oxygen-containing groups of GO nanosheets. Water molecules at the boundaries would suffer strong friction forces in comparison to water molecules in the center, resulting in a lower velocity as shown in Fig. S9 and Fig. S10. This velocity profile agrees with that predicted by the Poiseuille's law (please see discussion below Fig. S10 in the SD). Our simulation results also show that the central region has lower water density (see Fig. S11 in the SD). This suggests that less density region would possess higher water velocity under the same pressure.

The triangularly shaped nanochannels in MIL-140A are formed by hydrophilic ZrO_2 building units and hydrophobic organic linkers [65]. Fig. 8a shows that water molecules tend to concentrate at the centers of the nanochannels in MIL-140A, and some water molecules also accumulate around O atoms of the hydrophilic ZrO_2 units near the nanochannel surface. Correspondingly, Fig. 8b indicates that water molecules transport significantly faster at the center of nanochannels. Fig. 8a shows that fewer water molecules exist near benzene rings on the surface due to their hydrophobic nature. As shown in Fig. S12 in the SD, the cross-section nanochannel of MIL-140A shows an isosceles triangle shape profile. The two equal sides both contain benzene rings aligned along the water transport direction with a gap of 4 Å between two adjacent benzene rings. The plane formed by the benzene rings tilts 27° relative to the water transport direction. The base of the triangle contains 3-benzene ring stacks with a position mismatch of around 0.5 Å among the

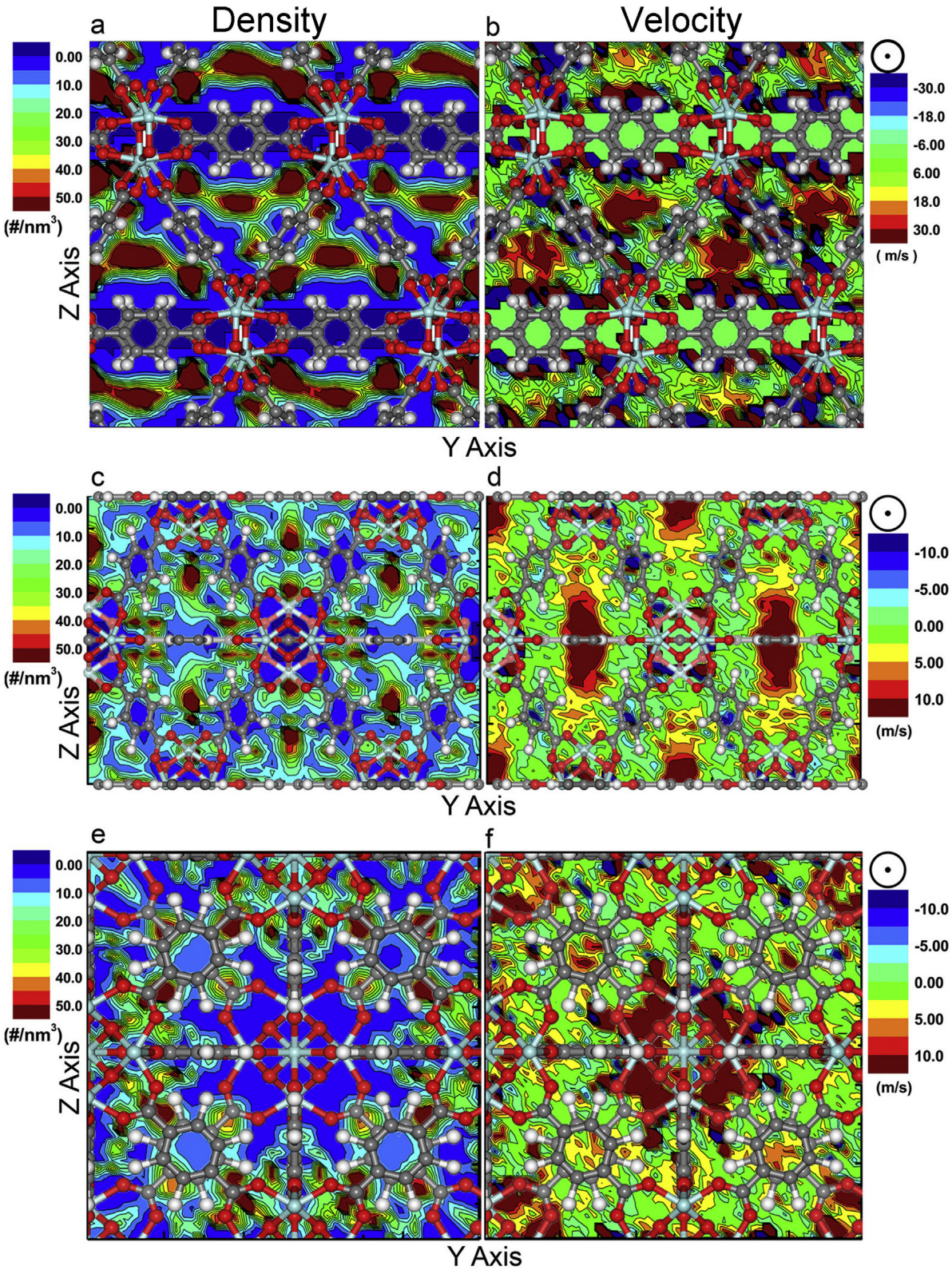

Fig. 8. 2D water molecular density (a, c, e) and velocity profiles (b, d, f) in (a, b) MIL-140A (direction 1), (c, d) UiO-66 (direction 1), and (e, f) UiO-66 (direction 2). Vertical and horizontal axis are Y and Z axis. Pressures are applied along + X axis. For density profiles, the warmer color corresponds to higher density. For velocity profiles, the warmer color corresponds to higher velocity along the +X axis, and the cooler color corresponds to higher velocity along X-axis. Zr (cyan), C (grey), O (red), and H (white) atoms are shown to illustrate the structure of MOFs. (A colour version of this figure can be viewed online.)

three benzene rings. Multiple benzene ring stacks sit along the water transport direction with a gap of 4 Å between two adjacent benzene ring stacks in the nanochannel. The planes formed by the benzene ring stacks are perpendicular to the water transport direction. Due to their misalignment with the water transport direction, these benzene rings function as "brushes" on the nanochannel surface, which would impede the transport of water molecules. Water molecules near such molecularly rough boundaries usually have small translational velocity and high rotational velocity. Fig. 8b indicates that the water velocity near the surface containing benzene rings has the coolest color adjacent to the warmest color, suggesting turbulent flow near the surface. Overall, the water velocity near the molecularly rough surface is small, which is consistent with Poiseuille's law.

In contrast to the regular triangular shaped nanochannels of MIL-140A, the shape of the UiO-66 (direction 1) nanochannel (Fig. 8c) is irregular, though its dimension is slightly larger than that of MIL-140A [40,42]. Most of the water molecules in the UiO-66 (direction 1) nanochannel concentrate at the top and bottom corners, suggesting a strong confinement effect at these locations. Fig. 8d indicates that a majority of water molecules move at a slow velocity, and only a few water molecules travel faster at the center of the nanochannel. In comparison, the UiO-66 (direction 2) nanochannel (Fig. 8e) is curved, which further increases water transport resistance. Fig. 8f shows that the low-velocity zones appear where most of the water molecules concentrate, resulting in a significantly lower overall water permeability in the nanochannels of UiO-66 than in MIL-140A. The velocity profiles in MOFs have also been plotted in Fig. S10. The positions of velocity peaks are consistent with the high-velocity regions shown in Fig. 8. These simulation results suggest that water transport is strongly influenced by the shape, molecular roughness and dimension of the nanochannels in MOFs.

3.4. Discussion on the roles of MOF spacers in graphene membranes

The simulation of water flow in this study was carried out under no-slip continuum hydrodynamics. As aforementioned, the experimental and theoretical simulation results show a good agreement with the changing trend of water permeability in the GO nanochannels with/without MOFs, providing strong evidence that the continuum hydrodynamics are suitable for estimating water transport properties in laminar GO membranes. Also, the simulation results indicate that water molecules in nanochannels of laminar GO membranes behave significantly different from those in hydrophobic channels such as that of carbon nanotubes or reduced GO [66–68]. The difference can be attributed to the fact that there is no curvature-induced low interfacial friction on the flat GO surface, and that the abundant surface functional groups on the hydrophilic GO surface create strong interactions with water molecules [69].

Our simulation results also show that water transport is sensitive to the roughness, shape, and dimension of nanochannels formed by MOFs (Fig. 8). Specifically, water can only travel along one direction in MIL-140A among the three possible directions, resulting in a water permeability coefficient of only 4.90 L m $^{-2}$ h $^{-1}$ bar $^{-1}$. Even though water can pass through both directions in UiO-66, their water permeability coefficients at 0.48 and 1.02 L m $^{-2}$ h $^{-1}$ bar $^{-1}$ are much lower than in the nanochannels of GO membranes. Most hydro-stable MOFs, such as the MIL-140 series, ZIF series, and HKUST-1, have rough, irregular and narrow nanochannels. Compared with the smooth hydrophobic inner channels of carbon nanotubes or biological pores such as aquaporins [70,71], MOFs cannot provide fast water transport channels without appropriate surface functionalization.

On the other hand, when MOF nanoparticles are intercalated among GO nanosheets, they serve more as filler materials in the composite (mixed-matrix) GO membranes. Based on our simulation results, water travels through MOF nanoparticles much slower than in GO nanochannels as consistently demonstrated by the decrease in water permeability coefficients (Fig. 5) when a small mass loading of MOFs is added. Owing to this difference in water transport resistance, these MOF nanoparticles impede rather than enhance water transport in laminated GO membranes. However, when the mass ratio of MOF to GO raises to 0.3 and higher, we observed a significant increase in water permeability, which is correlated to the increase in the interlayer spacing between GO nanosheets (see XRD results in Fig. 6). It is noteworthy to mention that our simulation results in Fig. 7 indicate a 5 times surge in water permeability when the interlayer spacing increases marginally from 0.82 to 1.06 nm. The large increase suggests that the water permeability of laminar GO membranes can change significantly if their average interlayer spacing is varied.

Based on the above experimental and simulation results, we propose models illustrated in Fig. 9 to explain how water transport behaviors vary in laminar GO membranes when MOF nanoparticles are intercalated. Essentially, GO nanosheets are flexible, and their interlayer spacing would change based on how the GO nanosheets flex. The interlayer spacing would expand to envelop the intercalated MOF nanoparticles. However, at regions without MOF nanoparticle intercalation, the interlayer spacing collapses back to afford constricted nanochannels just like those in pristine GO membranes (Fig. 9a). Due to the intercalation of MOF nanoparticle, these constricted nanochannels inevitably exhibit a larger interlayer spacing in comparison to pristine GO membranes as evidenced by our XRD results (Fig. 6). As shown in Fig. 9a and b, the water transport is expected to be non-uniform throughout the nanochannels with slow water transport through the intrinsic pores of the MOF nanoparticles (Fig. 9c) and faster transport through the constricted regions of the nanochannels. At low MOF loadings, the overall water permeability decreases because the stretches of fast water transport through the constricted nanochannels are unable to overcome the high transport resistance through the intrinsic pores of the MOF nanoparticles. On the other hand, the high transport resistance as a result of MOF nanoparticles intercalation can be offset by stretches of much faster water transport as driven by the enlarged interlayer spacing at higher MOF loadings (Fig. 9b). Hence, overall water permeability starts to increase after a particular threshold loading is reached. Furthermore, owing to the molecularly unsmooth surface and random orientations of the intercalated MOF nanoparticles, interfacial gaps tend to exist between the GO nanosheets and MOF nanoparticles (Fig. 9c), especially at high MOF loadings. This is evidenced by the GO wrinkles around MOF nanoparticles as illustrated in Fig. 4. Such GO/MOF interfacial gaps are likely to serve as additional water transport channels, which contribute to the observed increase in water permeability. The morphological difference between MIL-140A and UiO-66 is expected to affect the formation of GO/MOF interfacial gaps. Plate-like MIL-140A that is structurally flat would induce narrower GO/MOF interfacial gaps in comparison to spherical UiO-66 nanoparticles. Moreover, MIL-140A has a lateral dimension of around 0.8–2 μm and a thickness of 60–70 nm. As compared to UiO-66, which is spherical with a diameter of 60–70 nm, the contact area between MIL-140A and GO nanosheets is significantly larger, resulting in a shorter length of the fast transport constrained nanochannels as shown in Fig. 9a. Hence, a larger contact area by flat MOFs (*i.e.*, MIL-140A) is likely to lower the water permeability coefficient. This accounts for the slight drop in water permeability coefficients of GO/MIL-140A–0.1 and GO/MIL-140A–0.2 as shown in Fig. 5. In this regard, we envision that the future research direction should focus

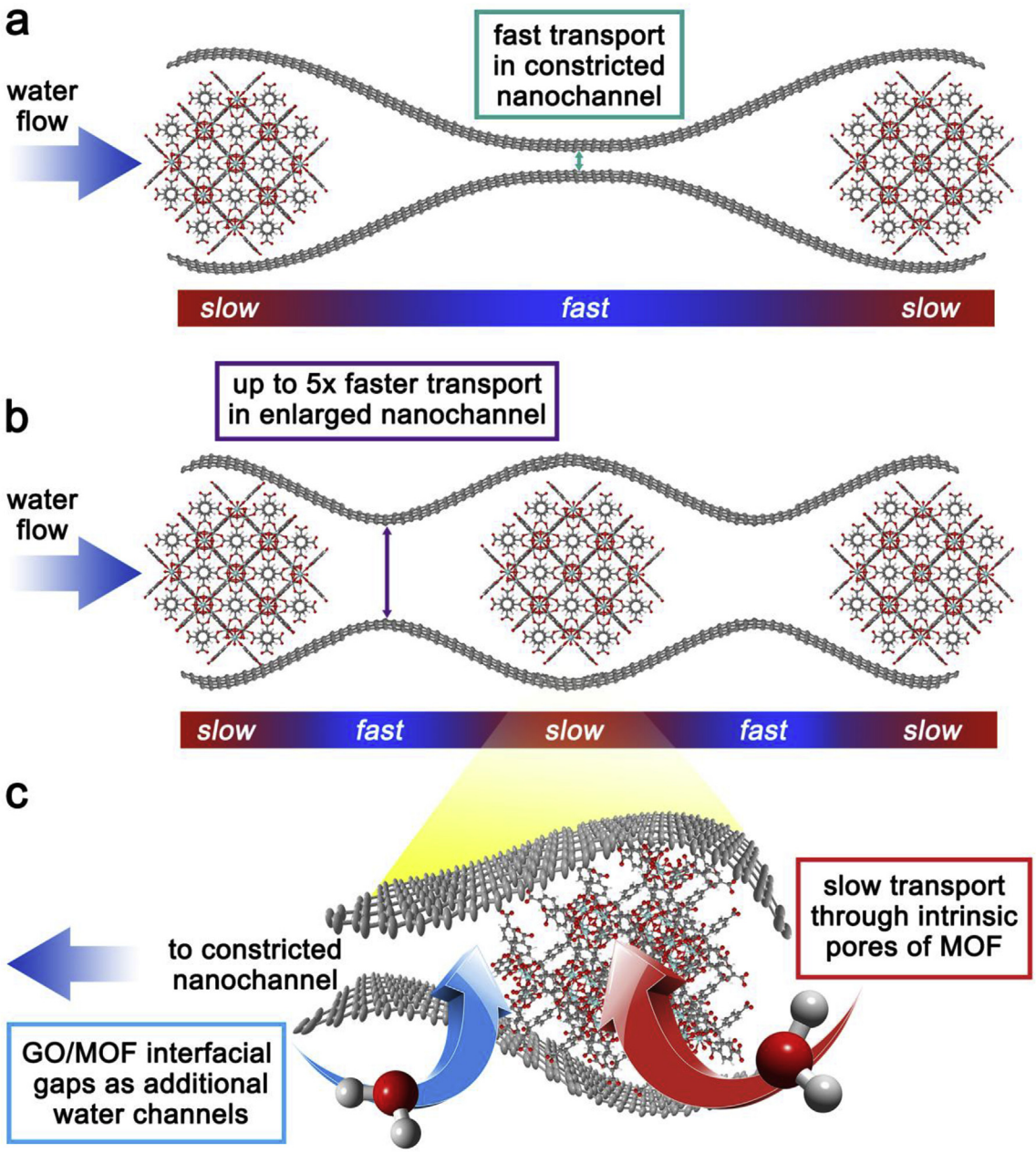

Fig. 9. Schematic illustration of water transport in MOF nanoparticle intercalated GO nanochannels. (a) Low mass loading of MOF nanoparticles, (b) high mass loading of MOF nanoparticles, and (c) interfacial gaps between MOF nanoparticles and GO nanosheets. (A colour version of this figure can be viewed online.)

on leveraging this unique GO/MOF architecture for potential selective adsorption for water treatment. The larger surface area and pore size of UiO-66 could be a potential good filler for such an application.

4. Conclusions

MOF particles have been proposed to serve as filler materials in laminar GO membranes to provide fast water transport channels for achieving enhanced water permeability. We demonstrated GO/MOF composite membranes by intercalating two types of water stable MOFs with different structures, namely, MIL-140A and UiO-66, into laminated GO membranes using a pressure assisted filtration method. Membrane characterization by SEM shows no signs of aggregation and that the MOF particles distributed uniformly among GO nanosheets without compromising the structural integrity of GO membranes. When a small number of MOFs (the weight ratio between MOF and GO below 0.3) is used, the water permeability decreases slightly. When a more significant amount of MOFs is added (at the weight ratio of 0.5), the water permeability increases significantly by 92% compared to that of GO membranes. We attributed this enhancement to the rise in the average interlayer spacing among GO nanosheets. MD simulation studies show that water molecules have strong interactions with different molecular components in the nanochannels in MOFs. The water permeability in MOFs depends on the shape, roughness, and dimension of the nanochannels in MOFs, and is in general much lower than that in the nanochannels between GO nanosheets. Counterintuitively, MOFs do not serve as fast water transport channels in GO membranes. Instead, a small loading of MOF

nanoparticles impedes water transport in nanochannels of GO membranes, resulting in a lower water permeability coefficient. On the other hand, a large loading of MOF particles can create very fast water transport stretches driven by the larger interlayer spacing. Besides, extra gaps may also be introduced between non-smooth MOF nanoparticles and GO nanosheets, serving as additional water transport channels to deliver higher water permeability. Overall, this work elucidates the role of intercalated MOFs in laminar GO membranes. Our results bespeak an important future research direction, which focuses instead on the selective adsorption capability of MOFs for potential water treatment applications.

Acknowledgments

The authors thank funding support from Australian Research Council under the Future Fellowships scheme (FT160100107 to Y.C. and FT170100283 to D.M.D.), Discovery Programme (DP180102210 to Y.C. and DP180103874 to D.M.D.), The University of Sydney Nano Institute under the Research Collaboration Award. H. D. also acknowledges support from the Australian Endeavour Leadership Program.

Appendix A. Supplementary data

Supplementary data to this article can be found online at https://doi.org/10.1016/j.carbon.2019.03.049.

References

[1] O.C. Compton, S.T. Nguyen, Graphene oxide, highly reduced graphene oxide, and graphene: versatile building blocks for carbon-based materials, Small 6 (2010) 711–723.
[2] S. Liu, T.H. Zeng, M. Hofmann, E. Burcombe, J. Wei, R. Jiang, J. Kong, Y. Chen, Antibacterial activity of graphite, graphite oxide, graphene oxide, and reduced graphene oxide: membrane and oxidative stress, ACS Nano 5 (2011) 6971–6980.
[3] R.R. Nair, H.A. Wu, P.N. Jayaram, I. V Grigorieva, A.K. Geim, Unimpeded permeation of water through helium-leak–tight graphene-based membranes, Science 335 (2012) 442–444.
[4] R.K. Joshi, P. Carbone, F.C. Wang, V.G. Kravets, Y. Su, I. V Grigorieva, H.A. Wu, A.K. Geim, R.R. Nair, Precise and ultrafast molecular sieving through graphene oxide membranes, Science 343 (2014) 752–754.
[5] K. Huang, G. Liu, Y. Lou, Z. Dong, J. Shen, W. Jin, A graphene oxide membrane with highly selective molecular separation of aqueous organic solution, Angew. Chem. Int. Ed. 53 (2014) 6929–6932.
[6] G. Liu, W. Jin, N. Xu, Graphene-based membranes, Chem. Soc. Rev. 44 (2015) 5016–5030.
[7] C. Finnerty, L. Zhang, D.L. Sedlak, K.L. Nelson, B. Mi, Synthetic graphene oxide leaf for solar desalination with zero liquid discharge, Environ. Sci. Technol. 51 (2017) 11701–11709.
[8] M. Fathizadeh, W.L. Xu, F. Zhou, Y. Yoon, M. Yu, Graphene oxide: a novel 2-dimensional material in membrane separation for water purification, Adv. Mater. Interfaces 4 (2017) 1–16.
[9] H. Ding, G. Peng, S. Mo, D. Ma, S.W. Sharshir, N. Yang, Ultra-fast vapor generation by a graphene nano-ratchet: a theoretical and simulation study, Nanoscale 9 (2017) 19066–19072.
[10] C. Chen, Q.H. Yang, Y. Yang, W. Lv, Y. Wen, P.X. Hou, M. Wang, H.M. Cheng, Self-assembled free-standing graphite oxide membrane, Adv. Mater. 21 (2009) 3007–3011.
[11] M.J. Allen, V.C. Tung, R.B. Kaner, Honeycomb carbon: a review of graphene, Chem. Rev. 110 (2010) 132–145.
[12] Y. Zhu, S. Murali, W. Cai, X. Li, J.W. Suk, J.R. Potts, R.S. Ruoff, Graphene and graphene oxide: synthesis, properties, and applications, Adv. Mater. 22 (2010) 3906–3924.
[13] J. Lee, H.R. Chae, Y.J. Won, K. Lee, C.H. Lee, H.H. Lee, I.C. Kim, J.M. Lee, Graphene oxide nanoplatelets composite membrane with hydrophilic and antifouling properties for wastewater treatment, J. Membr. Sci. 448 (2013) 223–230.
[14] K.H. Thebo, X. Qian, Q. Zhang, L. Chen, H.M. Cheng, W. Ren, Highly stable graphene-oxide-based membranes with superior permeability, Nat. Commun. 9 (2018) 1–8.
[15] B. Mi, Graphene oxide membranes for ionic and molecular sieving, Science 343 (2014) 740–742.
[16] S. Zheng, Q. Tu, J.J. Urban, S. Li, B. Mi, Swelling of graphene oxide membranes in aqueous solution: characterization of interlayer spacing and insight into water transport mechanisms, ACS Nano 11 (2017) 6440–6450.
[17] B. Chen, H. Jiang, X. Liu, X. Hu, Water transport confined in graphene oxide channels through the rarefied effect, Phys. Chem. Chem. Phys. 20 (2018) 9780–9786.
[18] J. Deng, Y. You, H. Bustamante, V. Sahajwalla, R.K. Joshi, Mechanism of water transport in graphene oxide laminates, Chem. Sci. 8 (2017) 1701–1704.
[19] A.R. Koltonow, J. Huang, Two-dimensional nanofluidics, Science 351 (2016) 1395.
[20] B. Chen, H. Jiang, X. Liu, X. Hu, Observation and analysis of water transport through graphene oxide interlamination, J. Phys. Chem. C 121 (2017) 1321–1328.
[21] B. Chen, H. Jiang, X. Liu, X. Hu, Molecular insight into water desalination across multilayer graphene oxide membranes, ACS Appl. Mater. Interfaces 9 (2017) 22826–22836.
[22] H.B. Park, J. Kamcev, L.M. Robeson, M. Elimelech, B.D. Freeman, Maximizing the right stuff: the trade-off between membrane permeability and selectivity, Science 356 (2017) 1337.
[23] J. Abraham, K.S. Vasu, C.D. Williams, K. Gopinadhan, Y. Su, C.T. Cherian, J. Dix, E. Prestat, S.J. Haigh, I.V. Grigorieva, P. Carbone, A.K. Geim, R.R. Nair, Tunable sieving of ions using graphene oxide membranes, Nat. Nanotechnol. 12 (2017) 546–550.
[24] C.N. Yeh, K. Raidongia, J. Shao, Q.H. Yang, J. Huang, On the origin of the stability of graphene oxide membranes in water, Nat. Chem. 7 (2015) 166–170.
[25] Y. Wei, Y. Zhang, X. Gao, Z. Ma, X. Wang, C. Gao, Multilayered graphene oxide membrane for water treatment: a review, Carbon 139 (2018) 964–981.
[26] W. Wang, E. Eftekhari, G. Zhu, X. Zhang, Z. Yan, Q. Li, Graphene oxide membranes with tunable permeability due to embedded carbon dots, Chem. Commun. 50 (2014) 13089–13092.
[27] K. Goh, W. Jiang, H.E. Karahan, S. Zhai, L. Wei, D. Yu, A.G. Fane, R. Wang, Y. Chen, All-carbon nanoarchitectures as high-performance separation membranes with superior stability, Adv. Funct. Mater. 25 (2015) 7348–7359.
[28] Y. Han, Y. Jiang, C. Gao, High-flux graphene oxide nanofiltration membrane intercalated by carbon nanotubes, ACS Appl. Mater. Interfaces 7 (2015) 8147–8155.
[29] X. Chen, M. Qiu, H. Ding, K. Fu, Y. Fan, A reduced graphene oxide nanofiltration membrane intercalated by well-dispersed carbon nanotubes for drinking water purification, Nanoscale 8 (2016) 5696–5705.
[30] K. Guan, D. Zhao, M. Zhang, J. Shen, G. Zhou, G. Liu, W. Jin, 3D nanoporous crystals enabled 2D channels in graphene membrane with enhanced water purification performance, J. Membr. Sci. 542 (2017) 41–51.
[31] Y. Ying, D. Liu, W. Zhang, J. Ma, H. Huang, Q. Yang, C. Zhong, High-Flux graphene oxide membranes intercalated by metal–organic framework with highly selective separation of aqueous organic solution, ACS Appl. Mater. Interfaces 9 (2017) 1710–1718.
[32] X. Li, Y. Liu, J. Wang, J. Gascon, J. Li, B. Van Der Bruggen, Metal-organic frameworks based membranes for liquid separation, Chem. Soc. Rev. 46 (2017) 7124–7144.
[33] Y.S. Bae, O.K. Farha, J.T. Hupp, R.Q. Snurr, Enhancement of CO_2/N_2 selectivity in a metal-organic framework by cavity modification, J. Mater. Chem. 19 (2009) 2131.
[34] E.V. Perez, K.J. Balkus, J.P. Ferraris, I.H. Musselman, Mixed-matrix membranes containing MOF-5 for gas separations, J. Membr. Sci. 328 (2009) 165–173.
[35] Y.S. Bae, R.Q. Snurr, Development and evaluation of porous materials for carbon dioxide separation and capture, Angew. Chem. Int. Ed. 50 (2011) 11586–11596.
[36] H.T. Kwon, H.K. Jeong, A. Mcferrin, In situ synthesis of thin Zeolitic–Imidazolate framework ZIF-8 membranes exhibiting exceptionally high propylene/propane separation, J. Am. Chem. Soc. 6 (2013) 12.
[37] D. Liu, X. Ma, H. Xi, Y.S. Lin, Gas transport properties and propylene/propane separation characteristics of ZIF-8 membranes, J. Membr. Sci. 451 (2014) 85–93.
[38] Y. Hu, J. Wei, Y. Liang, H. Zhang, X. Zhang, W. Shen, H. Wang, Zeolitic imidazolate framework/graphene oxide hybrid nanosheets as seeds for the growth of ultrathin molecular sieving membranes, Angew. Chem. Int. Ed. 55 (2016) 2048–2052.
[39] W.J. Koros, C. Zhang, Materials for next-generation molecularly selective synthetic membranes, Nat. Mater. 16 (2017) 289–297.
[40] W. Liang, R. Babarao, T.L. Church, D.M. D'Alessandro, Tuning the cavities of zirconium-based MIL-140 frameworks to modulate CO_2 adsorption, Chem. Commun. 51 (2015) 11286–11289.
[41] H. Zhang, J. Hou, Y. Hu, P. Wang, R. Ou, L. Jiang, J.Z. Liu, B.D. Freeman, A.J. Hill, H. Wang, Ultrafast selective transport of alkali metal ions in metal organic frameworks with subnanometer pores, Sci. Adv. 4 (2018).
[42] W. Liang, C.J. Coghlan, F. Ragon, M. Rubio-Martinez, D.M. D'Alessandro, R. Babarao, Defect engineering of UiO-66 for CO_2 and H_2O uptake – a combined experimental and simulation study, Dalton Trans. 45 (2016) 4496–4500.
[43] W. Liang, D.M. D'Alessandro, Microwave-assisted solvothermal synthesis of zirconium oxide based metal-organic frameworks, Chem. Commun. 49 (2013) 3706–3708.
[44] C. Vieira Soares, D. Damasceno Borges, A. Wiersum, C. Martineau, F Nouar, P.L. Llewellyn, N.A. Ramsahye, C Serre, G Maurin, A.A. Leitã, Adsorption of small molecules in the porous zirconium-based metal organic framework MIL-140a (Zr): a joint computational-experimental approach, J. Phys. Chem. C 120 (2016) 7192–7200.
[45] S. Friebe, B. Geppert, F. Steinbach, J. Rgen Caro, Metal–Organic framework UiO-66 layer: a highly oriented membrane with good selectivity and

hydrogen permeance, ACS Appl. Mater. Interfaces 9 (2017) 12878–12885.
[46] S. Plimpton, Fast parallel algorithms for short-range molecular dynamics, J. Comput. Phys. 117 (1995) 1–19.
[47] D. Ma, H. Ding, H. Meng, L. Feng, Y. Wu, J. Shiomi, N. Yang, Nano-cross-junction effect on phonon transport in silicon nanowire cages, Phys. Rev. B 94 (2016), 165434.
[48] J.L.F. Abascal, C. Vega, A general purpose model for the condensed phases of water: TIP4P, J. Chem. Phys. 123 (2005), 234505.
[49] William L. Jorgensen, A. David S. Maxwell, J. Tirado-Rives, Development and testing of the OPLS all-atom force field on conformational energetics and properties of organic liquids, J. Am. Chem. Soc. 118 (1996) 11225–11236.
[50] T.R. Cundary, M.S. Gordon, UFF, a full periodic table force field for molecular mechanics and molecular dynamics simulations, J. Am. Chem. Soc. 114 (1992) 10024–10035.
[51] S.L. Mayo, B.D. Olafson, W.A.G. Iii, DREIDING: a generic force field for molecular simulations, J. Phys. Chem. 94 (1990) 8897–8909.
[52] M. Prakash, H. Jobic, N.A. Ramsahye, F. Nouar, D. Damasceno Borges, C. Serre, G. Maurin, Diffusion of H_2, CO_2, and their mixtures in the porous zirconium based metal–organic framework MIL-140a(Zr): combination of quasi-elastic neutron scattering measurements and molecular dynamics simulations, J. Phys. Chem. C 119 (2015) 23978–23989.
[53] D. Cohen-Tanugi, L.C. Lin, J.C. Grossman, Multilayer nanoporous graphene membranes for water desalination, Nano Lett. 16 (2016) 1027–1033.
[54] Z. Hu, Y. Chen, J. Jiang, Zeolitic imidazolate framework-8 as a reverse osmosis membrane for water desalination: insight from molecular simulation, J. Chem. Phys. 134 (2011), 134705.
[55] C.H. Tsou, Q.F. An, S.C. Lo, M. De Guzman, W.S. Hung, C.C. Hu, K.R. Lee, J.Y. Lai, Effect of microstructure of graphene oxide fabricated through different self-assembly techniques on 1-butanol dehydration, J. Membr. Sci. 477 (2015) 93–100.
[56] L.J. Cote, J. Kim, Z. Zhang, C. Sun, J. Huang, Tunable assembly of graphene oxide surfactant sheets: wrinkles, overlaps and impacts on thin film properties, Soft Matter 6 (2010) 6096.
[57] X. Shen, X. Lin, N. Yousefi, J. Jia, J.K. Kim, Wrinkling in graphene sheets and graphene oxide papers, Carbon 66 (2014) 84–92.
[58] F. Kim, L.J. Cote, J. Huang, Graphene oxide: surface activity and two-dimensional assembly, Adv. Mater. 22 (2010) 1954–1958.
[59] J.Y. Chong, B. Wang, K. Li, Water transport through graphene oxide membranes: the roles of driving forces, Chem. Commun. 54 (2018) 2554–2557.
[60] F. Wang, Y. You, X. Jin, R. Joshi, On the Role of Driving Force for Water Transport through Nanochannels within Graphene Oxide Laminates, Nanoscale 10 (2018) 21625–21628.
[61] S. Park, K.S. Lee, G. Bozoklu, W. Cai, S.T. Nguyen, R.S. Ruoff, Graphene oxide papers modified by divalent ions enhancing mechanical properties *via* chemical cross-linking, ACS Nano 2 (2008) 572–578.
[62] J.A. Thomas, A.J.H. McGaughey, Reassessing fast water transport through carbon nanotubes, Nano Lett. 8 (2008) 2788–2793.
[63] Y.H. Cho, H.W. Kim, H.D. Lee, J.E. Shin, B.M. Yoo, H.B. Park, Water and ion sorption, diffusion, and transport in graphene oxide membranes revisited, J. Membr. Sci. 544 (2017) 425–435.
[64] W.L. Xu, C. Fang, F. Zhou, Z. Song, Q. Liu, R. Qiao, M. Yu, Self-Assembly: a facile way of forming ultrathin, high-performance graphene oxide membranes for water purification, Nano Lett. 17 (2017) 2928–2933.
[65] A.D. Wiersum, E. Soubeyrand-Lenoir, Q. Yang, B. Moulin, V. Guillerm, M. Ben Yahia, S. Bourrelly, A. Vimont, S. Miller, C. Vagner, M. Daturi, G. Clet, C. Serre, G. Maurin, P.L. Llewellyn, An evaluation of UiO-66 for gas-based applications, Chem. An Asian J. 6 (2011) 3270–3280.
[66] G. Hummer, J.C. Rasaiah, J.P. Noworyta, Water conduction through the hydrophobic channel of a carbon nanotube, Nature 414 (2001) 188–190.
[67] J.K. Holt, H.G. Park, Y. Wang, M. Stadermann, A.B. Artyukhin, C.P. Grigoropoulos, A. Noy, O. Bakajin, Fast mass transport through sub–2-nanometer carbon nanotubes, Science 312 (2006) 1034–1037.
[68] H. Huang, Z. Song, N. Wei, L. Shi, Y. Mao, Y. Ying, L. Sun, Z. Xu, X. Peng, Ultrafast viscous water flow through nanostrand-channelled graphene oxide membranes, Nat. Commun. 4 (2013) 2979.
[69] K. Falk, F. Sedlmeier, L. Joly, R.R. Netz, L. Bocquet, Lpmcn, Molecular origin of fast water transport in carbon nanotube membranes: superlubricity versus curvature dependent friction, Nano Lett. 10 (2010) 4067–4073.
[70] H. Gyu Park, Y. Jung, Carbon nanofluidics of rapid water transport for energy applications, Chem. Soc. Rev. 43 (2014) 565.
[71] H. Sui, B.G. Han, J.K. Lee, P. Walian, B.K. Jap, Structural basis of water-specific transport through the AQP1 water channel, Nature 414 (2001) 872–878.